Superconducting penetration depth of Aluminum thin films

Superconductor
Science and
Technology

PAPER • **OPEN ACCESS**

Superconducting penetration depth of aluminum thin films

To cite this article: David López-Núñez *et al* 2025 *Supercond. Sci. Technol.* **38** 095004

OPEN ACCESS
IOP Publishing
Superconductor Science and Technology
Supercond. Sci. Technol. **38** (2025) 095004 (16pp)
https://doi.org/10.1088/1361-6668/adf360

Superconducting penetration depth of aluminum thin films

David López-Núñez[1,2,3], Alba Torras-Coloma[1,4], Queralt Portell-Montserrat[1,4,5], Elia Bertoldo[1], Luca Cozzolino[1], Giovanni Alberto Ummarino[6,7], Alessio Zaccone[8], Gemma Rius[5], M Martínez[1,9] and P Forn-Díaz[1,9,*]

[1] Institut de Física d'Altes Energies, The Barcelona Institute of Science and Technology, Bellaterra 08193, Spain
[2] Departament de Física Quàntica i Astrofísica and Institut de Ciències del Cosmos, Universitat de Barcelona, Barcelona 08028, Spain
[3] Barcelona Supercomputing Center, Barcelona 08034, Spain
[4] Departament de Física, Universitat Autònoma de Barcelona, 08193 Bellaterra, Spain
[5] Institute of Microelectronics of Barcelona (IMB-CNM), Spanish National Research Council (CSIC), Cerdanyola 08193, Spain
[6] Dipartimento di Scienza Applicata e Tecnologia, Politecnico di Torino, Corso Duca degli Abruzzi 24, 10129 Torino, Italy
[7] National Research Nuclear University MEPhI (Moscow Engineering Physics Institute), Kashira Hwy 31, Moskva 115409, Russia
[8] Department of Physics 'A. Pontremoli', University of Milan, via Celoria 16, 20133 Milan, Italy
[9] Qilimanjaro Quantum Tech SL, Barcelona, Spain

E-mail: pforndiaz@ifae.es

Received 5 March 2025, revised 24 May 2025
Accepted for publication 22 July 2025
Published 11 September 2025

Abstract

We present a study of the superconducting penetration depth λ in aluminum thin films of varying thickness. The range of thicknesses chosen spans from the thin-film regime to the regime approaching bulk behavior. The penetration depths observed range from $\lambda = 163 \pm 1$ nm for the thinnest 28 nm samples down to $\lambda = 58 \pm 1$ nm for the 207 nm-thick ones, allowing us to provide an estimate of the thickness at which aluminum becomes a type-I superconductor. In order to accurately determine λ, we performed complementary measurements using the frequency of superconducting *LC* resonators obtained through novel and efficient methods of fitting and simulation, as well as the normal-state resistance of meandered structures. Both methods yield comparable results, providing a well-characterized set of values of λ in aluminum in the relevant range for applications in fields such as quantum computing and microwave radiation detector technologies.

Keywords: penetration depth, superconducting qubits, superconducting resonators

* Author to whom any correspondence should be addressed.

1. Introduction

Bulk aluminum has been an extensively studied material in the literature [1], often considered as the archetype of conventional type-I superconductivity. In contrast, the properties of thin-film aluminum, conventionally utilized in, e.g. quantum computing technologies [2–5] and kinetic inductance detectors [6], are not as widely apparent. Specifically, thin-film aluminum exhibits type-II superconductivity [7], resulting in a complete different behavior than its bulk version.

In type-II superconductors, the short range of Cooper pairs results in the emergence of normal-metal paths, leading to the appearance of vortices within the material [8]. Furthermore, type-II superconductors may exhibit a significantly large kinetic inductance, L_k, comparable or larger than their geometric inductance, L_g [9, 10]. Accurately determining L_k is important as it needs to be taken into account, e.g. in the design of quantum circuits [10, 11], requiring a thorough material characterization, particularly concerning the superconducting penetration depth, λ. This parameter is intrinsically material-dependent and represents the distance a parallel magnetic field penetrates into a superconductor. External factors such as the presence of impurities, the thickness of the film, or the direction of the magnetic field lead to an effective value of λ [12]. In particular, the film thickness strongly influences microscopic properties such as the electrical resistivity and the electron mean-free path [13–15], which then modify the value of λ. To the best of our knowledge, the relationship between thickness and penetration depth in aluminum in the range of thicknesses targeted in our study has not been extensively documented in the existing literature [16].

In this work, we determine the penetration depth of thin-film aluminum samples across film thicknesses in the range 28–207 nm, with the goal of providing a well-characterized set of values of λ for thin-film aluminum usable in the design of, e.g. resonating structures or circuits to build qubits [4, 5, 10]. This determination is accomplished through two complementary methods: measurement of the resonance frequency of a number of lumped-element superconducting resonators, and by evaluation of the resistance of thin-film test structures. These methodologies align with previous investigations conducted on other superconducting materials, such as Nb [17], NbN [18] and granular aluminum [19]. In addition to λ, both methods combined allow us to characterize L_k for all thicknesses studied. Therefore, the results obtained in this work and the methods developed are an important resource in the design of thin-film aluminum-based circuits. In order to properly evaluate λ, we have developed a new fitting method for resonator devices with accurate error estimation, as well as a simulation technique using an EM solver to efficiently account for finite thickness effects in the estimation of the inductance. Finally, our investigation yields an estimate of the range of film thicknesses at which the transition occurs between the type-II superconductivity exhibited by thin-film aluminum and the type-I superconductivity characteristic of vortex-free, bulk aluminum. This transition may be relevant for superconducting qubits [20, 21] and resonators [7] since the presence of vortices alters the quality of devices made of thin-film aluminum.

The outline of this work is as follows: section 2 introduces the theoretical aspects of superconductivity needed for the data analysis. In section 3, the methods used in this work to extract the penetration depth λ are described. Section 4 presents the simulation methods along with the device characteristics. Section 5 focuses on the experimental implementation. The experimental results are discussed in section 6. Finally, section 7 presents the conclusions of this work.

2. Theoretical background

In general, the superconductivity type exhibited by a given material is an expression of the interplay between the superconducting penetration depth λ and its coherence length ξ, which corresponds to the average distance between the electrons forming a Cooper pair [22].

The thickness of a thin film is manifested in the values of its internal microscopic parameters, as variations of both λ and ξ and the rest of parameters that depend on them. In particular, the kinetic inductance L_k has a strong dependence on λ through [19, 23–25]

$$L_k = L_{k,s} N = \mu_0 \lambda N, \tag{1}$$

where $L_{k,s}$ is the kinetic inductance per square. N is the number of squares of a given wire. For wires with constant cross section, we have $N = g/w$, where g and w are the wire length and width, respectively. Otherwise, N has to be calculated along the wire.

In bulk aluminum, the response of the superconductor to magnetic fields is non-local, causing λ to be larger than the one predicted by the London equations $\lambda_L = 15.7$ nm. Since the Al bulk coherence length is $\xi_0 = 1.6\,\mu\text{m} \gg \lambda_L$, bulk aluminum is in the non-local limit. In the non-local limit, λ is modified by [12]

$$\lambda = 0.65 \left(\lambda_L^2 \xi_0\right)^{1/3}, \tag{2}$$

which, in the case of bulk aluminum, it is $\lambda_{bulk} = 50$ nm [12, 26]. Thus, bulk aluminum satisfies type-I superconductivity criteria, $\xi_0 > \lambda_{bulk}$.

However, in polycrystalline aluminum, decreasing the film thickness d eventually decreases the grain size as well [27], thereby reducing the electron mean free path, l. In this regime, an effective coherence length $\xi < \xi_0$ at $T = 0$ K can be defined [12, 28]

$$\frac{1}{\xi} = \frac{1}{\xi_0} + \frac{1}{l}. \tag{3}$$

The presence of impurities also reduces l and, consequently, ξ is reduced as well [12]. In this thin film regime, the BCS theory

predicts the following expression of λ at zero temperature [8]

$$\lambda = \lambda_{\mathrm{L}}(0)\sqrt{1+\frac{\xi_0}{l}}, \tag{4}$$

where $\lambda_{\mathrm{L}}(0) \equiv \lambda_{\mathrm{L}}$ is the London penetration depth at $T = 0\,\mathrm{K}$. Thus, by lowering d, one may arrive at the regime where $\xi < \lambda$, causing a change of superconductivity to a type-II superconductor, where the response to external fields is local. The transition between superconductivity regimes is determined by the Ginzburg–Landau parameter κ [8]

$$\kappa \equiv \lambda/\xi. \tag{5}$$

Above $\kappa = 1/\sqrt{2}$, the superconductor is type-II since the normal-superconductor interface energy becomes negative, thus allowing for the generation of normal paths (vortices) [29]. For thick enough films, κ decreases below $1/\sqrt{2}$ and the film exhibits vortex-free behavior, thus entering the type-I superconductivity regime. By carefully engineering the thicknesses of different thin films, this boundary between superconductivity types occurring at a critical thickness d_{c} may be attained. In actual thin films, local fluctuations in κ are expected given the typically disordered nature of the film, thus leading to a spread of values of d_{c} over which the transition takes place.

For very thin films where $d \lesssim \lambda$ the response of the film to external perpendicular magnetic fields follows the London equations, causing an opposing current $\vec{j}_S$ to an incoming field $\vec{A}_S$. Since d is so small, the magnetic field fully penetrates the film. Nevertheless, the expression $\vec{j}_S = -\frac{\mu_0}{\lambda^2}\vec{A}_S$ remains valid [30]. The correction to $L_{\mathrm{k,s}}$ in this regime valid for very thin films is given by [24]

$$L_{\mathrm{k,s}} = \mu_0\lambda\coth\frac{d}{\lambda} \equiv \mu_0\lambda_{\mathrm{thin}}, \tag{6}$$

where λ_{thin} is an effective penetration depth. For $d \gg \lambda$, $\lambda_{\mathrm{thin}} \to \lambda$, while for $d \ll \lambda$, $\lambda_{\mathrm{thin}} \to \frac{\lambda^2}{d}$, significantly enhancing $L_{\mathrm{k,s}}$. Resonator measurements, as will be detailed in the next section, give direct access to L_{k}, which can be used to derive λ_{thin} through equation (6), and then converted to λ.

An alternative method of estimating λ results from using the Einstein relation connecting the electron mean-free path l to the residual normal state resistivity ρ_n as [31, 32]

$$l = \frac{m v_{\mathrm{F}}}{e^2 n \rho_n}. \tag{7}$$

Here, m is the electron mass, v_{F} is the Fermi velocity, e is the electron charge, and n is the density of free carriers. Combining this expression with equation (4), leads to the expression [17]

$$\lambda\,(\mathrm{nm}) = 99.5\sqrt{2.5\times10^{-2} + \rho_n\,(\mu\Omega\cdot\mathrm{cm})}. \tag{8}$$

Therefore, the value of λ obtained through equation (6) may be validated by resistance measurements on thin films of the same nominal thickness d.

Equations (6) and (8) allow a complete characterization of λ and L_{k} of thin superconducting films, and are the basis of the experiment in this work.

3. Methodology to extract λ

Following from the previous section, two independent approaches are here proposed and implemented to estimate λ in aluminum thin films. The first method involves resonator measurements combined with EM simulation, where the effect of λ is reflected in the measured resonance frequency. The second approach utilizes four-probe measurements on resistive aluminum meanders.

The resonator measurements give access to λ through λ_{thin}, while the resistance measurements give direct access to λ. Fabrication inaccuracies affect both methods differently. Discrepancies between nominal and real dimensions are much more difficult to track in resonators than in four-probe designs. λ_{thin} is also much more sensitive to deviations in the thickness d. Appendix F contains a thorough investigation of the uncertainties in the parameters to yield the error in λ from both methods.

3.1. Resonance method

Lumped element LC resonators were chosen for this study in order to achieve a more controlled definition of their inductance L and capacitance C, compared to distributed resonators. LC resonators are characterized by their resonance frequency $\omega = (LC)^{-1/2}$, where C represents the capacitance and $L = L_{\mathrm{g}} + L_{\mathrm{k}}$ is the sum of geometric and kinetic inductances. As explained in section 2, superconductors may exhibit a significantly high L_{k}, especially for thin films with $d \ll \lambda$ [10].

In order to extract L_{k}, we first perform an accurate simulation of each resonator studied considering a perfect conductor, thus obtaining L_{g} and C that lead to a simulated resonance frequency f_{sim} (figure 1(a) with $L_{\mathrm{k}} = 0$). The value of the simulated frequency f_{sim} already contains the dispersive effect from coupling to the measurement line. Resonator measurements provide f_{meas} as they contain a total inductance $L = L_{\mathrm{g}} + L_{\mathrm{k}}$ (figure 1(a)), so $f_{\mathrm{sim}} > f_{\mathrm{meas}}$ (figure 1(b)). L_{k} may be then obtained with

$$L_{\mathrm{k}} = L_{\mathrm{g}}\left(\frac{f_{\mathrm{sim}}^2}{f_{\mathrm{meas}}^2} - 1\right). \tag{9}$$

The L_{k} obtained in this way determines λ_{thin} using equation (6). This method requires a precise simulation of the perfect conductor resonance f_{sim} (see section 4).

3.2. Resistivity method

Resistance measurements directly lead to λ through equation (8). Since ρ_n is the normal state resistivity at 0 K, it can only be measured by destroying the superconducting state with an external magnetic field. However, the aluminum resistivity is nearly constant at low

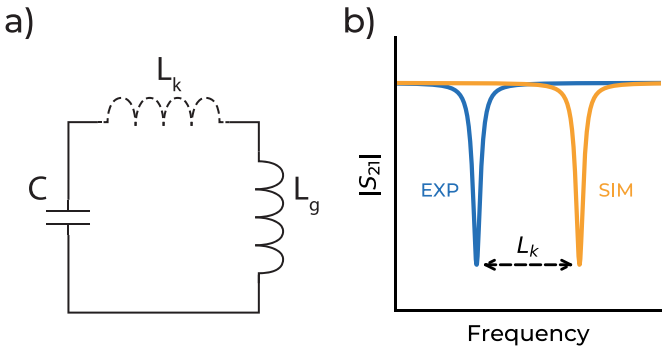

Figure 1. (a) *LC* Resonator circuit schematic. In the simulations conducted, no kinetic inductance is considered, while in the experiment the kinetic inductance L_k contribution adds to the geometric inductance, $L_{exp} = L_k + L_g$. (b) Simulated and experimental resonances are assumed to only deviate due to L_k.

temperatures, so we instead approximate ρ_n with the value at 4 K [1].

It is important to note that ρ_n is connected to λ and not to λ_{thin} as in the resonator method. ρ_n and λ are connected through the intrinsic properties of the material, such as the charge carrier mass, the Cooper pair number density, and the electron mean free path. Accordingly, the thin-film effects described in equation (6) do not play a role in the determination of λ through ρ_n.

4. Resonator simulations and device characteristics

In this section, we summarize the procedure we followed to perform simulations on the resonator circuits, followed by the device characteristics.

First, for each film thickness d, we employ FastHenry[10] to obtain an estimate of the kinetic inductance fraction $\alpha \equiv L_k/L$. We work in the range $\alpha = 0.02$–0.5, as lower α can incur in big inaccuracies in λ, while higher α leads to frequencies lower than our experimental system bandwidth (4–8 GHz). FastHenry allows an independent extraction of L_g by setting $\lambda = 0$. Then, we assume an exponential behavior of $\lambda(d)$, leading to an estimate of $\alpha(d)$. More details can be found in appendix D. These simulations allow us to determine the inductor wire width w in each resonator for a given d.

Next, we employ Sonnet[11] to run an entire resonator simulation to obtain the system transmission (see appendix D for details on the simulations). In these simulations we use the value of the electrical permittivity $\epsilon_r = 11.45$, validated in [33] which was also the low-temperature value confirmed by the wafer manufacturer [35]. As seen in figure 2(a), the value of the resonance changes noticeably for values of ϵ_r found throughout the literature, leading to a difference in the

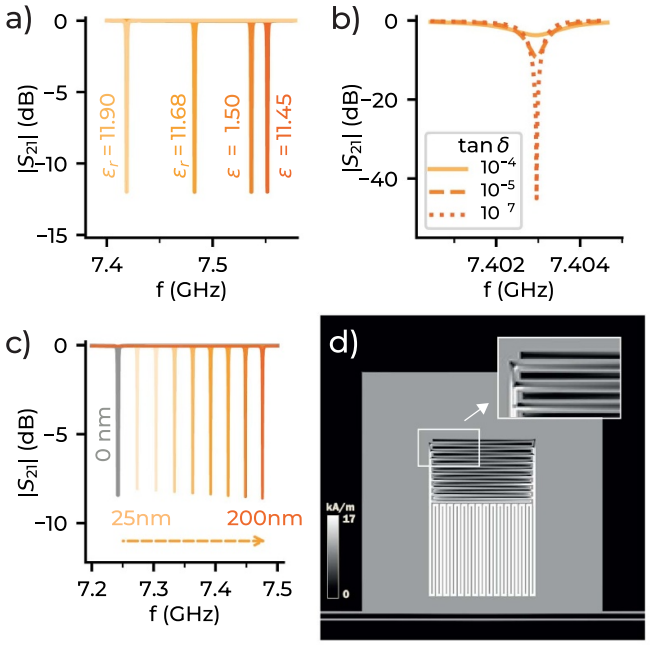

Figure 2. Sonnet simulations of the response of *LC* resonators on Si. (a) Simulated response with varying Si relative permittivity, ϵ_r. $\epsilon_r = 11.9$ corresponds to bulk Si. $\epsilon_r = 11.45$ is the value used in this work, being properly validated at low temperatures and at microwave frequencies [33]. (b) Effect of Si loss tangent, $\tan\delta$, on the quality factor of *LC* resonators. Upper bound obtained using values from [34]. (c) Sonnet simulations for a small resonator transmission. Grey curve represents the default response, i.e. for no finite metal thickness. Yellow and increasing saturation color curves correspond to thicknesses ranging from 25 nm to 200 nm. (d) Simulated current distribution of a *LC* resonator. The inset shows the current in the last capacitor fingers, where it is minimal.

obtained λ of up to 100%. Adding realistic values of substrate loss $\tan(\delta)$ [34] to the simulations did not change the resonance frequency appreciably (see figure 2(b)). Therefore, we can conclude that the presence of surface lossy dielectrics, while they significantly impact the internal quality factor of resonators, will only affect the values of λ obtained in this work below the 1% level.

To discern the simulated values of L_g and C we follow the procedure described in [36]. A first simulation of the system yields the resonance frequency f_{sim}. The values of L_g and C are estimated with an additional simulation wherein a sheet inductance (L_s) is manually incorporated in a single square at the center of the inductor, leading to a modified resonance frequency $f'_{sim} = 1/(2\pi) \cdot [(L_g + L_s)C]^{-1/2}$. This procedure is equivalent to what is shown in figure 1(b), but with a manually incorporated L_k.

However, in actual films a larger thickness d decreases L_g combined with an increase in C. This thickness-dependence effect cannot be directly captured by Sonnet since it was originally designed to solve only planar structures. To obtain the effect of d on L_g and C in the simulation without resorting to slower, full 3D methods, the thickness is artificially incorporated in Sonnet simulations by including an additional aluminum layer containing the same resonator circuit above the

[10] We use the version found in www.wrcad.com/ftp/pub/fasthenry-3.0wr-071720.tar.gz which takes into account the London equations and thus the penetration depth λ in the inductance calculations.

[11] https://www.sonnetsoftware.com/.

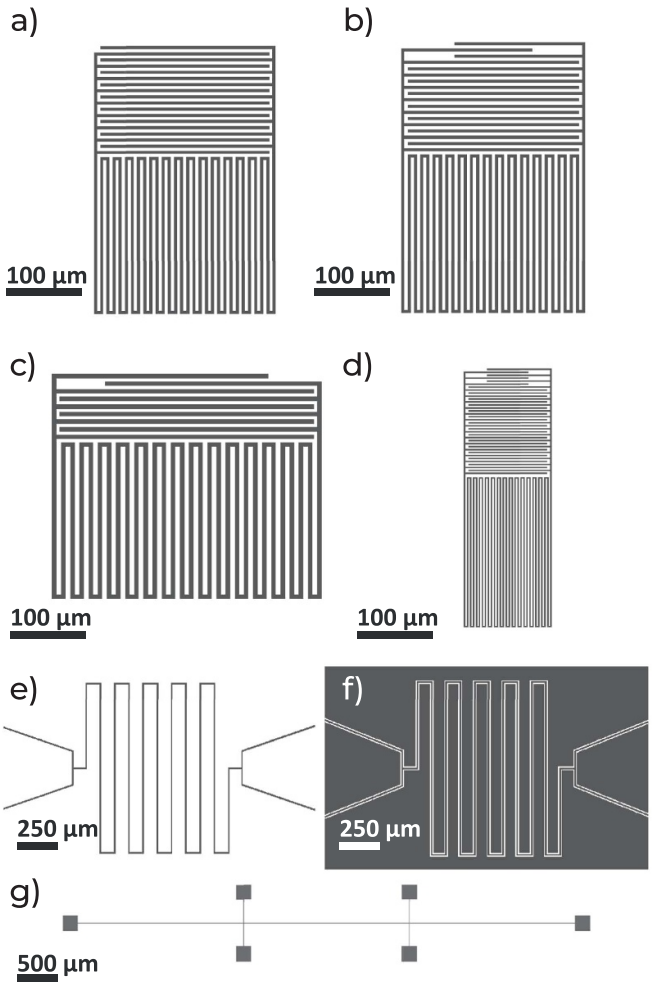

Figure 3. *LC* resonator device design variations: (a) medium; (b) medium with adjusted finger capacitor; (c) large, (d) and small. Design of a 4-probe measurement meander without (e) and with (f) surrounding ground plane. (g) Layout of a HB measurement.

existing structure and connecting both through vias along all edges. For the largest d considered (200 nm) the resulting correction due to thickness on the resonance frequency amounts to approximately 2% (figure 2(c)). We have actually validated this method against a full 3D model. More details can be found in appendix D.

Three types of resonators were designed with varying line widths and line gaps to introduce different contributions of L_k. The three designs are named small resonators (SRs), medium resonators (MRs), and large resonators (LRs), each with a meander and capacitor widths of 2, 4, and 6 μm, respectively (see figures 3(a)–(d)). LR are suited for higher L_k contribution while SR are suited for larger thickness.

The lumped description with isolated L and C is justified with the current simulations (figure 2(d)), where most of the current is present in the meander. Using current simulations as the one shown in figure 2(d), we estimate that 98% of the energy is located inside the inductor meander. The extra 2% is taken into account to obtain an effective length of the meander for computing the number of squares N in equation (1). Moreover, the ground plane is designed sufficiently far from the resonator so we can neglect its contribution to the inductance.

In order to have better statistics in the value of λ for a given thickness, resonators with the same L and different C are designed. This is obtained by changing the outermost fingers of the capacitor (figures 3(a)–(d)), where there is nearly no contribution to L (see inset of figure 2(d)). In figure 3(b) an example of an MR with the last fingers modified is shown. This modification of the finger reduces C, thus increasing the resonance frequency. Resonators are sufficiently spaced in frequency to be experimentally distinguishable (>25 MHz) in the range 7–8 GHz.

For the four-probe measurements, a long meander structure was designed (see figures 3(e) and (f)). Two different meanders were considered, with and without ground plane around the meander. The size of the meander was chosen to ensure that the resistance at 4 K falls within a measurable range of 100 Ω–1 kΩ. A horizontal bar structure (HB) has also been used (see figure 3(g)) as a complementary measurement of resistance.

The thicknesses d chosen for the study range from 25 nm to 200 nm. This range includes typical values found for superconducting qubit devices and radiation detectors (50–100 nm). Including this range is indispensable for calibrating λ for real-scenario devices. $d < 50\,\text{nm} \sim \lambda_{\text{bulk, Al}}$ is chosen to observe thin-film effects, while $d > 100$ nm is chosen to explore the regime approaching bulk aluminum behavior. The actual thicknesses were accurately determined using atomic force microscopy.

The devices were fabricated using photolitography on high-resistivity $\rho_{\text{Si}} > 100\,\text{k}\Omega\cdot\text{cm}$ Si wafers (see [35] for more details on wafer parameters) with the aluminum deposited by electron-beam evaporation. The chips were later diced and devices were bonded with aluminum wires to a ceramic printed circuit board (PCB), or to a chip carrier in the case of four-probe devices. Images from actual devices can be seen in figures 4(a) and (b). More details regarding thin film fabrication can be found in appendix B, including images of three samples of increasing thickness, also displaying a clear increase of apparent grain size.

Two different evaporators, one Plassys at IFAE and another from Univex at CNM, were used in this study in order to account for possible fabrication dependencies on λ. While the IFAE evaporator is only used for aluminum, the CNM evaporator processes additional metals. We note that both metal deposition systems are routinely used to fabricate high-quality superconducting qubits and resonators. Therefore, we do not expect a high level of impurities in the resulting thin films that may otherwise impact λ [12].

Altogether, the different variety of designs and fabrication conditions account for potential systematic variability on λ, ensuring a more comprehensive analysis.

5. Experiment

All resonator devices were mounted in a sample holder at the mixing chamber plate of a dilution refrigerator ($T =$

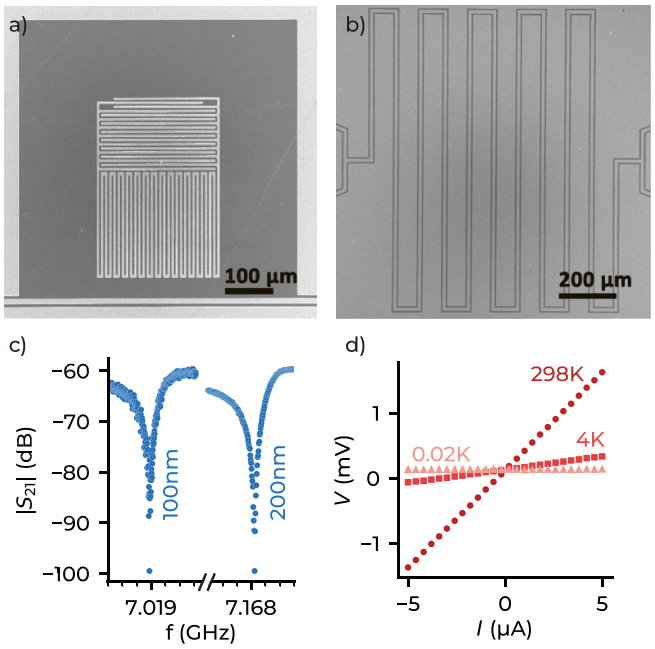

Figure 4. (a) Scanning electron micrograph (SEM) of a *LC* resonator. (b) SEM of a meander structure measured by 4-probe method. (c) S_{21} data and fit of measured resonators with 100 nm and 200 nm thickness. Each minor tick corresponds to 1 MHz (d) Resistance measurements at room temperature (RT), 4 K and 20 mK.

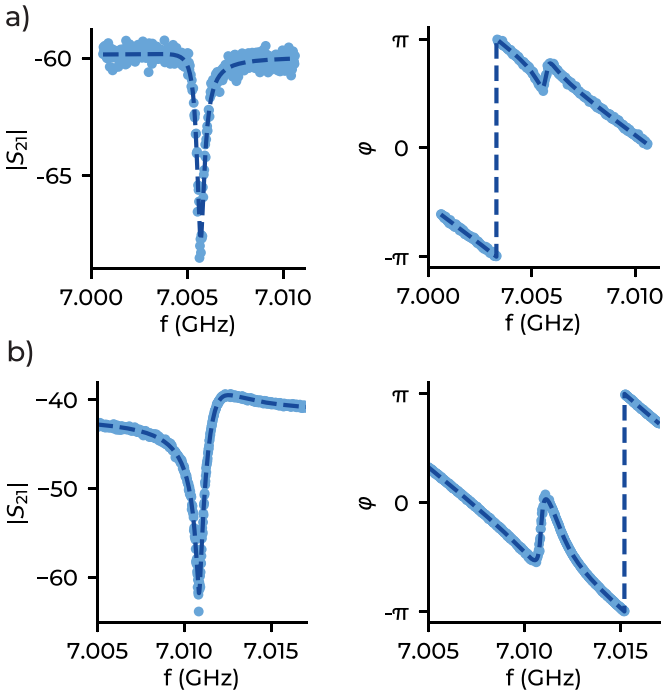

Figure 5. S_{21} resonator response in magnitude ($|S_{21}|$, left) and phase (φ, right). The fit using our procedure is superimposed to the light blue data points as a dark blue dashed line. (a) 100 nm-thick MR resonator. (b) 200 nm-thick MR resonator, with the same design as the device in (a), probed at higher power.

20 mK) and subjected to measurements using a vector network analyzer at estimated power levels near the single photon regime, with 10 Hz integration frequency bandwidth and 10 averages per trace. The full measurement setup schematics can be found in appendix A. 4-probe structures were either located in the same chip as the resonators or in a separate chip, in which case they were located either at the mixing chamber or at the still plate of the dilution refrigerator.

Resistance measurements were performed at room temperature and at 4 K (see figure 4(d)). Then, a continuous acquisition was run at a low current while sweeping the temperature around $T_{C,bulk} \sim 1.2$ K to reach the critical temperature of the sample. T_C was determined at the midpoint of the superconductor-normal transition where the resistance dropped by 50%. More details on the extraction process of T_C is given in appendix C, including a summary plot of all estimated values of T_C obtained as function of thickness, which are also reported in table 2 below.

A typical resonator measurement is shown in figure 4(c) for two different resonator thicknesses. The resonator response was fit to the following expression [37]

$$S_{21} = a e^{i\alpha} e^{-2\pi i f \tau} \left[1 - \frac{(Q_l/|Q_c|)\, e^{i\phi}}{1 + 2iQ_l\,(f/f_r - 1)} \right], \qquad (10)$$

where the factor between brackets is the actual resonator response, while the pre-factor in front accounts for the response of the rest of the circuit. a is an attenuation constant, α represents a phase shift, τ is the electrical delay of the measurement line, and f_r is the resonator frequency. Q_l is the loaded quality factor related to the complex coupling quality factor $Q_c \equiv |Q_c| e^{i\phi}$ and internal quality factor Q_i through $Q_l^{-1} = Q_i^{-1} + \mathrm{Re}(Q_c^{-1})$ [37]. ϕ expresses the impedance mismatch. Typical fits to the resonator response are shown in figures 5(a) and (b), where one can see that the impedance mismatch is correctly captured.

Our fitting process follows from a routine inspired by [37]. In that study, the data fitting is performed sequentially, until the full expression for S_{21} is obtained. However, with such a sequential process it is hard to propagate errors in the fitting, and correlations between parameters are lost. For that reason, we use the sequential procedure to yield our initial parameter guess. Once an initial set of parameters is obtained, we use the iminuit library [38] for fitting the full S_{21} expression. Iminuit is a library mainly used by the particle physics community, with a focus on error propagation and accurate uncertainty estimation. The S_{21} fit has seven parameters, which makes it a complex fit, and proper error estimation becomes relevant. In most fits, the initial guess and final fitting parameters were close. In general, having good initial parameters for iminuit is indispensable. In some resonators, however, iminuit fitting found a considerably better solution than the initial one, while providing a correct error estimation.

Table 1 shows fitted parameters from resonators in figure 5, with the corresponding errors. The relative error in frequency δf_r is of order 10^{-6}, which is the most important parameter to extract λ. The resonator internal quality factor Q_i is not used in this study. In fact, the resonators in this work are designed with $Q_l \ll Q_i$ to maximize the signal strength, and therefore Q_i

Table 1. Results of the fits from figure 5. All parameters are used in equation (10) to fit the resonator response. Parameter uncertainties are obtained using iminuit, as detailed in the main text. $|Q_c|$ and Q_l are related through $Q_l^{-1} = Q_i^{-1} + \mathrm{Re}(Q_c^{-1})$ [37].

Res. ID	f_r (GHz)	δf_r (kHz)	$\lvert Q_c\rvert$	$\delta\lvert Q_c\rvert$	Q_l	δQ_l	ϕ	$\delta\phi$	α	$\delta\alpha$	a	δa	τ(Hz)	$\delta\tau$(Hz)
0	7.0056	8	$1.52\cdot10^4$	$3\cdot10^2$	$9.2\cdot10^3$	200	0.22	0.02	−3.78	0.04	$1.01\cdot10^{-3}$	$3\cdot10^{-6}$	$6.97\cdot10^{-8}$	$7\cdot10^{-11}$
1	7.0115	1	$3.47\cdot10^3$	2	$4.2\cdot10^3$	3	−0.76	0.001	−2.87	0.001	$8.17\cdot10^{-3}$	$1\cdot10^{-6}$	$6.99\cdot10^{-8}$	$5\cdot10^{-14}$

Table 2. Results for both resistance and resonance frequency measurements. d_{nom} is the nominal target thickness, while d_{meas} is the measured thickness using atomic force microscopy. λ is the measured average penetration depth. Measurement type is 'LC' for lumped resonators and '*R*' for 4-probe resistance measurements. '*N*' represents the number of devices measured for each particular thickness, which include small resonators (SRs), medium resonators (MRs), and large resonators (LRs) for the resonance frequency measurements, and four-probe (4P), and HB geometry for the resistance measurements. The fabrication facility is specified for each device. For resonator measurements, λ_{thin} is shown, together with surface kinetic inductance $L_{k,s}$. For resistance measurements, residual-resistance ratio, defined as $RRR = R_{RT}/R_{4K}$ is shown. In all resonator measurements the system temperature was 20 mK.

Device id	d_{nom}(nm)	d_{meas}(nm)	λ(nm)	Meas.	Design	*N*	Fab.	λ_{thin}(nm)	$L_{k,s}$ (fH)	*RRR*	T_C(K)
1	25	28 ± 4	163 ± 1	LC	MR	9	IFAE	965 ± 12	1212 ± 5	—	—
2	25	28 ± 4	178 ± 3	R	4P	1	IFAE	—	—	2.1 ± 0.1	1.32 ± 0.03
3	50	52 ± 2	118 ± 1	LC	MR	9	IFAE	286 ± 4	359 ± 2	—	—
4	75	73 ± 2	94 ± 1	LC	MR	5	IFAE	145 ± 3	182 ± 3	—	—
5	75	76 ± 3	89 ± 1	R	4P	1	CNM	—	—	4.8 ± 0.1	1.22 ± 0.01
6	75	78 ± 3	97 ± 3	LC	LR	9	IFAE	145 ± 7	182 ± 3	—	—
7	100	97 ± 3	83 ± 1	R	4P	1	CNM	—	—	6.1 ± 0.1	1.27 ± 0.02
8	100	105 ± 2	76 ± 2	LC	MR	5	IFAE	87 ± 3	109 ± 3	—	—
9	100	105 ± 2	63 ± 1	LC	LR	5	IFAE	67 ± 1	84 ± 3	—	—
10	100	105 ± 2	73 ± 1	R	4P	1	IFAE	—	—	7.2 ± 0.1	—
11	100	105 ± 2	73 ± 1	R	HB	1	IFAE	—	—	7.2 ± 0.1	—
12	100	127 ± 5	63 ± 3	LC	SR	9	CNM	65 ± 4	83 ± 2	—	—
13	100	127 ± 5	70 ± 1	R	4P	1	CNM	—	—	7.4 ± 0.1	1.22 ± 0.05
14	200	188 ± 3	58 ± 2	LC	MR	5	IFAE	58 ± 3	73 ± 2	—	—
15	200	188 ± 4	58 ± 1	R	4P	1	IFAE	—	—	11.6 ± 0.1	1.20 ± 0.02
16	200	207 ± 5	59 ± 2	LC	MR	6	CNM	59 ± 2	74 ± 2	—	—
17	200	207 ± 5	58 ± 1	R	4P	1	CNM	—	—	9.9 ± 0.1	1.20 ± 0.05

is not very accurately determined, lying in the range 10^3–10^4. The thickness dependence of Q_i will be examined in future work.

6. Results

The obtained values of λ for each sample thickness d from both resonator and resistance measurements are plotted in figure 6. Each point of the resonator measurement is obtained by an average of several resonators on the same chip with varying capacitance and kinetic inductance ratio (see table 2), as explained in section 4. The vertical error bars correspond to the standard error of the mean. The error in the horizontal axis corresponds to the uncertainty of the film thickness due to its granular nature. The resistance measurements are taken on a single structure in each device, with the vertical error bar corresponding to the error in the fitting of the resistance (figure 4). The complete error propagation analysis is detailed in apprendix F.

Table 2 shows the full set of experimental results obtained for both the resonance and resistance measurements. A total of 70 structures have been analyzed, combining the two measurement methods (see section 3), three different designs for each measurement method, along with eight different thicknesses and two evaporation facilities. This combination reduces considerably the possibility of a systematic error on the experiment, and provides a good statistical ensemble from which to extract conclusive values of λ.

The data in figure 6 exhibit a consistent trend, with λ increasing rapidly for $d < 100$ nm and approaching bulk values for $d \sim 200$ nm, validating the chosen thickness range. The two methods to extract λ predict values differing by less than 10% for all thicknesses studied, giving more confidence to the experimental results obtained.

The resonance frequency method gives access to L_k through equation (9), which is then converted to $L_{k,s}$ via equation (1). $L_{k,s}$ is proportional to λ_{thin}, and both are shown in figure 7(a). In this figure, only *LC* resonators are plotted, and the exponential increase at low thicknesses is more pronounced than the increase of λ in figure 6, as expected. Large $L_{k,s}$ values near ∼10 pH are predicted for aluminum with $d \sim 10$ nm. Combined with a long enough meander, pure aluminum can

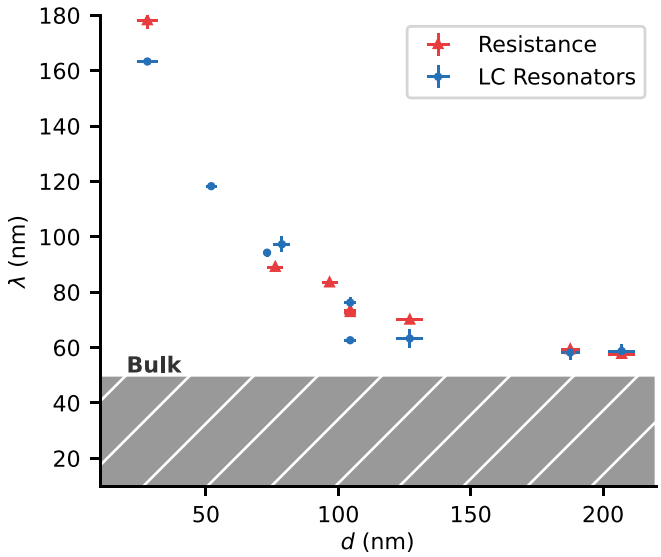

Figure 6. Measured penetration depth λ as a function of device thickness d. Two measurement methods are shown: resistance measurements (red triangles) and *LC* resonator resonances (blue circles). Bulk penetration depth is shown as a lower limit. The thickness of samples is measured using atomic force microscopy.

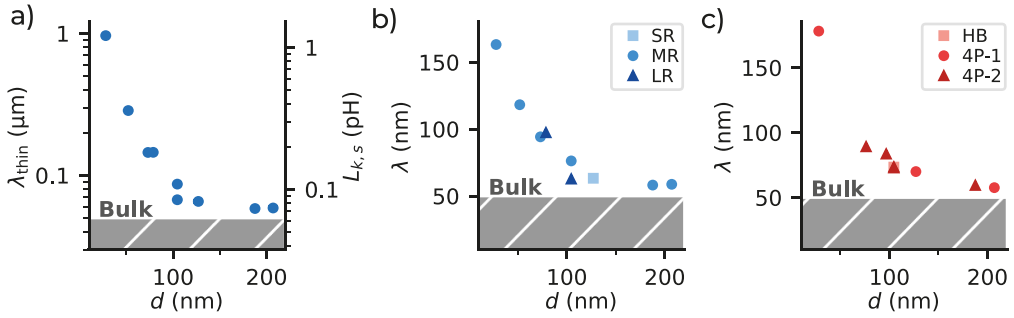

Figure 7. (a) *LC* resonator response, plotted in two scales: λ_{thin} (left y-axis) and L_{k} (right y-axis), which are proportional, see equation (6). (b) Measured λ by the resonance frequency method for different thicknesses. Different resonator types are shown. (c) Measured λ using the resistance method for different thicknesses. Different resistance structures are shown, the two types of four-probe measurements, with (4P-1) and without (4P-2) ground plane, and the HB geometry.

attain L_{k} values comparable to those exhibited by superinductors [39].

Figure 7(b) shows variations in the design for the resonance measurements. The noticeable difference in the values of λ at $d = 100\,\text{nm}$ in figure 7(b) may arise from a systematic difference in the device geometry between *M* and *L* resonators not accounted for.

Resistance measurements are displayed in figure 7(c). Most data are obtained from 4-probe structures with (4P-1) and without (4P-2) surrounding ground plane. The single HB geometry value is consistent with the rest of 4-probe measurements. Devices fabricated at different fabrication facilities did not show visible deviations in λ despite exhibiting different values of the residual resistance ratio *RRR* (table 2).

The results obtained in this work allow us to provide estimates of the critical thickness d_{c} where aluminum turns from a type-I to a type-II superconductor. Such a transition is expected to occur for a value of $\kappa = \lambda/\xi = 1/\sqrt{2}$ in equation (5) [29]. Figure 8 shows the estimated values of κ as a function of thickness d using equations (3) and (7), leading to $d_{\text{c}} \simeq 100\,\text{nm}$. An exact description of l and, therefore, κ as a function of d will be the subject of future work.

As argued in section 2, the actual transition between superconductivity types may take place over a certain range of values of d_{c}, given the intrinsic inhomogeneity of κ due to the disordered nature of thin films. In summary, our results suggest that the thicker samples ($d > 100\,\text{nm}$, device id 14–17) may enter the regime towards type-I superconductivity [40], unlike the thinner ones ($d < 100\,\text{nm}$, device id 1–13) which are more likely to behave as type-II local superconductors.

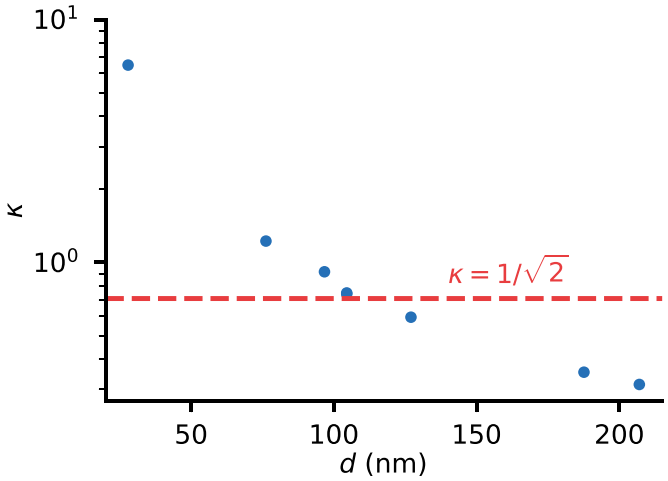

Figure 8. Estimated dependence of $\kappa \equiv \lambda/\xi$ on thickness, combining equations (3), (7) and (5). According to this estimate, the transition between superconductivity regimes, when $\kappa = 1/\sqrt{2}$ (red horizontal dashed line) [29], occurs at a critical thickness $d_c \simeq 100\,\text{nm}$.

7. Conclusions

In this work, we performed a characterization of the aluminum penetration depth λ for thicknesses in the range 28–207 nm. The values of λ obtained range from 163 nm for the thinnest samples down to 58 nm, approaching the aluminum bulk value for the thickest films. Our measurements of λ as function of thickness represent a guide to superconducting circuit designs where inductance plays a significant role, such as, e.g. circuit QED and kinetic inductance detectors.

We have also introduced an accurate fitting procedure for resonators which can easily be extended to other experimental settings. For simultaneous parameter fits, sequential fitting can be a good process to obtain each parameter at a time. However, this process does not provide a good estimation of the fitting error and the correlations between parameters. Using the result of sequential fitting as the initial guess, we then fitted with the iminuit package, providing an accurate error estimation and, in particular instances, a better parameter prediction.

Our work has also allowed us to provide an estimate of the thickness value at which thin-film aluminum starts to behave as a type-I superconductor, to lie close to 100 nm. This value is obviously inaccurate but it helps to narrow down the range of thicknesses in future studies interested in analyzing the transition region. Further work is needed to explore the actual transition point by, e.g. measuring the coherence length as function of thickness or even directly imaging the presence of vortices, as in [41]. One can then investigate potential new circuit functionalities in thicker aluminum films, such as quasiparticle traps using the dependence of the superconducting gap on thickness [42, 43] or the exclusion of vortices in sufficiently thick films. The effect of, for instance, a thicker ground plane may be validated in the coherence properties of flux-sensitive devices such as flux qubits [20].

Data availability statement

The data that support the findings of this study are openly available at the following URL/DOI: https://doi.org/10.1088/1361-6668/adf360.

Acknowledgments

We would like to give special thanks to Sonnet support software for their help in running our simulations, and Topsil for providing detailed specifications from our wafers. We also want to thank Qilimanjaro engineers David Eslava and Yifei Chen for their collaboration and help during measurements, and Prof. Teun Klapwijk and Prof. Teresa Puig for their insightful comments. D L N acknowledges support by an FPI grant from the Spanish Ministry of Science and Innovation (MICIN). We also acknowledge funding from the Ministry of Economy and Competitiveness and Agencia Estatal de Investigacion (RYC2019-028482-I, RyC-2026-21412, PCI2019-111838-2, PID2021-122140NB-C31, PID2021-122140NB-C32), the European Commission (FET-Open AVaQus GA 899561, QuantERA SiUCs and QRADES), and program 'Doctorat Industrial' of the Agency for Management of University and Research Grants (2020 DI 41; 2020 DI 42; 2024 DI 00004). The IMB-CNM is supported by the María de Maetzu grant for Centres of Excellence programme CEX2023-001397-M funded by MICIU/AEI/10.13039/501100011033. This work used the Spanish ICTS Network MICRONANOFAB. IFAE is partially funded by the CERCA program of the Generalitat de Catalunya. This study was supported by MICIN with funding from European Union NextGenerationEU (PRTR-C17.I1) and by Generalitat de Catalunya.

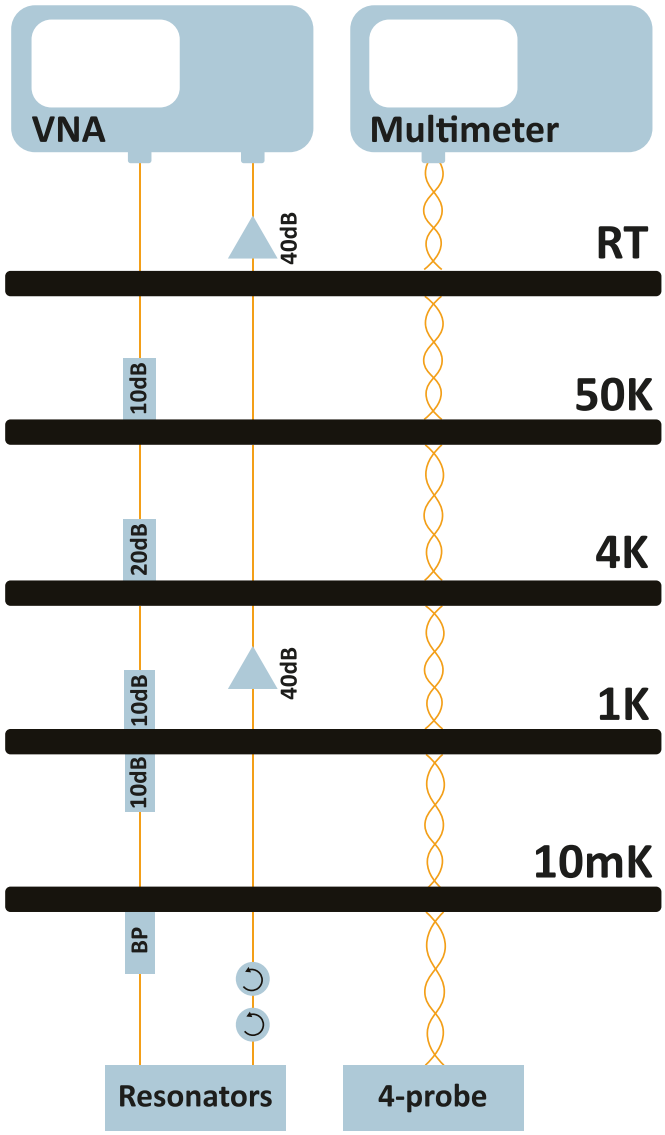

Figure 9. Measurement setup. High-frequency coaxial lines are attenuated 50 dB and filtered above 8 GHz. The output signal is passed through two circulators and amplified through a HEMT amplifier and a room temperature amplifier. Resonators were measured with an Agilent vector network analyzer E5071B. DC lines for resistance measurement were twisted pairs thermalized in several stages at the refrigerator. A Keithley 2600B source measurement unit was used for these measurements.

Appendix A. Experimental setup

The experimental setup used in the measurements of all devices presented in this work is shown in figure 9.

Appendix B. Fabrication

High resistivity silicon wafers from TOPSIL provider are used as substrates for all the fabricated devices. The basic processing steps for patterning the electronic devices are as follows.

Samples are diced as quarter wafers and subsequently cleaned in acetone, rinsed in isopropanol and blown dry in N_2 stream. Substrates are dehydrated before photoresist deposition. LOR3A plus HIPR-6512 resists are spin coated and soft baked sequentially. A Karl Suss mask aligner is used for resist-stack exposure and then a development sequence using ODP is applied. The pattern transfer consists in aluminum thin film deposition followed by a lift off of the resist in NMP solvent. The aluminum deposition was performed by e-beam evaporation for the given thicknesses. Figure 10 shows SEM images of different samples to observe the grain size. The remaining LOR3A is removed by mild oxygen plasma treatment. For electrical characterization, the samples were diced appropriately and mounted onto ceramic PCBs. Devices were wire-bonded with aluminum wires to either a sample holder for AC measurements or to chip carriers for DC measurements. Exemplary images of actual devices are shown in figures 4(a) and (b).

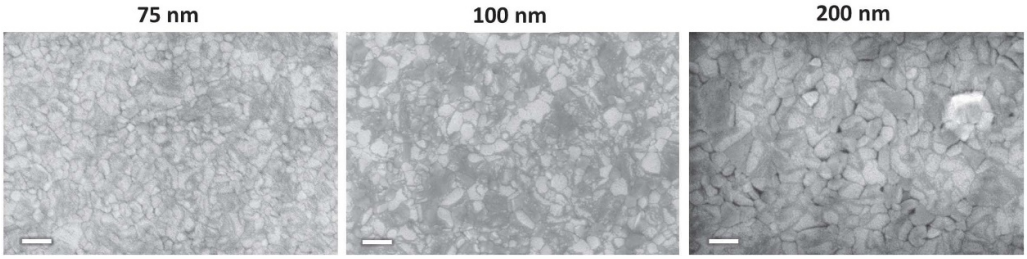

Figure 10. SEM Images for samples of increasing thickness illustrating the evolution in apparent grain size. The id of samples with 75 nm, 100 nm, and 200 nm correspond to 4, 9, 14, respectively. Scale bar corresponds to 200 nm.

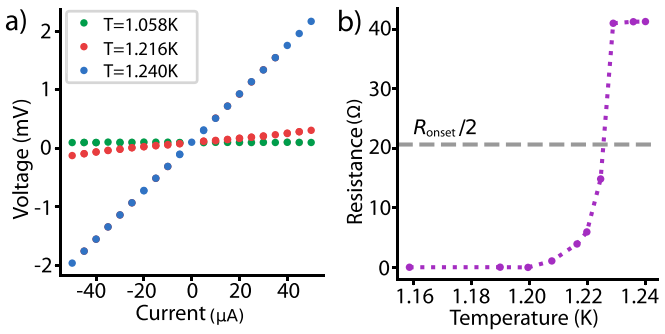

Figure 11. (a) I–V curve taken at different temperatures for a 127 nm-thick sample. (b) Fitted resistance at different temperatures. The horizontal dashed line marks the value where resistance drops by half, $R_{max}/2$, where T_C is defined.

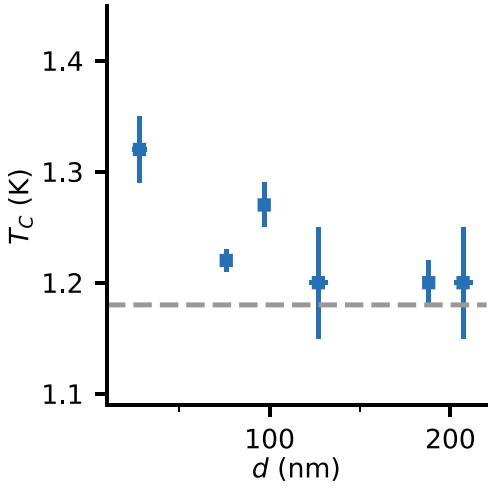

Figure 12. Critical temperature T_C of resistor samples at different thicknesses, as measured following the procedure described in the text and in figure 11.

Appendix C. T_C measurements

In order to characterize the critical temperature T_C of each sample measured in this work, I–V curves are taken while the fridge temperature is swept in a controllable fashion. Figure 11(a) shows I–Vs from three different temperatures for a sample 127 nm thick. The temperature is recorded simultaneously at each data point of the I–V curve. The value of the temperature used in the plots is then the average temperature across all the values of each I–V curve. This way we take into account possible heating effects due to the largest currents applied. A simple linear regression is used to obtain the resistance R. The results of fitted resistance as function average temperatures is shown in figure 11(b). The $R_{onset}/2$ marks the value at which T_C is defined, being a drop in resistance by a factor 2 from the temperature at which resistance starts to decrease suddenly.

In figure 12, the T_C dependence with sample thickness is shown. As expected, T_C is enhanced for lower thicknesses and approaches the bulk aluminum value for the thicker films, $T_C = 1.18$ K.

Appendix D. Simulations

FastHenry simulations were used to obtain an approximation of the kinetic inductance fractions of the resonator inductances, $\alpha \equiv L_k/L$. Those simulations determine the width and gap of the meanders, along with the number of meander turns.

For FastHenry simulations, the value of λ had to be estimated, since it is needed for estimating the kinetic inductance L_k. We fitted a phenomenological behavior of λ as a decaying exponential with base $\lambda_{bulk} = 50$ nm and known values from previous internal studies at $d = 25$ nm and $d = 50$ nm. The used expression is $\lambda(d)[\text{nm}] = \lambda_{bulk} + 196 \cdot e^{-d[\text{nm}]/74.3}$.

With the final results, setting 4 μm as the meander gap and width (which corresponds to MR-type resonators in section 4), for 25 nm thickness $\alpha = 0.47$ and for 200 nm, $\alpha = 0.03$, being the limits in thickness established for our work. LR- and SR-type resonators are designed for lower and higher thicknesses, respectively.

The main simulations were run with Sonnet, with 1 μm fine meshing. To obtain different resonators with different resonance frequency but the same value of L_k, only the last fingers of the inter-digitated capacitor were modified (see main text figure 3(b)), to keep the total inductance as constant as possible. The current in the last fingers of the capacitor is minimal (see main text figure 2(d)). This was easily achieved by parameterizing a Sonnet file and sweeping over the length of the last fingers. The frequency values obtained were approximately evenly spaced. The number of fingers modified and the distance between fingers was different for each resonator type (M, S and L).

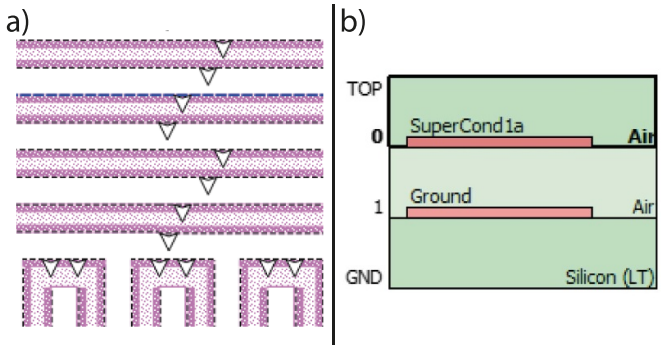

Figure 13. (a) Sonnet design to simulate thickness in resonator. (a) Zoom-in of the simulation design in a device like the one shown in figure 2(d), with the through vias represented as white triangles on the fingers (upper wires) and meanders (bottom turning wires) to connect the two layers of metal used to emulate thickness. (b) Sonnet layer list, where two metallic layers are placed to simulate the film thickness.

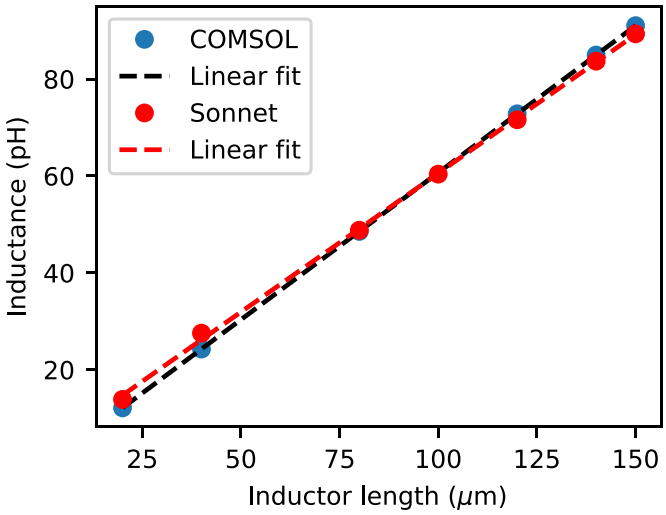

Figure 14. Simulated values of an inductor 4 μm wide, 100 nm thick using a full 3D model (COMSOL) and the thick-metal technique with Sonnet. Linear fits are added for visual aid. Both methods yield similar results with differences in the 1%–2% level.

When performing the simulation of a given resonator, not only the resonance frequency f_0 was acquired, but also the total inductance, L, and total capacitance, C. We followed the method described by Doyle *et al* [36], which consists on adding an extra known sheet inductance in a single square of the meander and obtaining a new modified frequency f_0'. Together with f_0 and the known added inductance value, L and C can be separately obtained. More details can be found in the main text section 3.1.

Finally, we need to add the thickness into the simulation. This is a sensitive parameter in LC resonators, as shown in figure 2(c) of the main text, where the difference between sheet metal (gray resonance) and the thickest sample (200 nm) was around 2%, comparable to the difference added due to L_k in real experiments for the thickest samples. In order to carry out the simulations, we followed a technique available within Sonnet that allows one to mimic thickness into an otherwise planar geometry, including the effect of sheet inductance[12]. In order to implement this technique, two layers of superconductor are added on top of the silicon, separated by a distance d. Then, these two layers are connected through vias along all the edges. This effectively creates a thick resonator, reducing the inductance and increasing the capacitance. This technique is significantly faster to simulate entire resonator circuits as compared to using full 3D finite element solvers. A zoom-in of the simulation design we developed, including the vias connecting the vertical dimension, can be seen in figures 13(a) and (b).

We have validated the technique by simulating a linear inductor of the dimensions of our resonators using both Sonnet as well as the AC/DC-package from COMSOL. The inductor dimensions are 4 μm wide, 100 nm thick, and a varying length. We first run COMSOL simulations of the inductor to determine a suitable set of parameters. Using the 'Finer' meshing setting the error induced in the value of the inductance is below 0.15%. We also find that a layer of 200 μm of Si substrate and 200 μm of air above the chip lead to sufficient values with error below 0.1% compared to thicker geometries. The Sonnet simulations are carried out with the same geometry of the inductor, substrate and air box, using the technique to connect two layers to simulate finite thickness. The meshing is set to 100 nm, based on the limit set by the accuracy of the width (see appendix B). The resulting inductances with both methods as function of length is shown in figure 14. The values differ from each other less than 2% in the worst cases, therefore justifying our simulation method. The simulation time of Sonnet for this inductor is a few seconds while it takes a few minutes for COMSOL, making it an advantageous technique.

Despite being more efficient than a full 3D simulation, these thick-metal Sonnet simulations required a significant amount of computer memory. In order to optimize simulation time, instead of simulating all the resonators with all the different finger lengths, for each resonator width, we only simulated the resonators with the shortest and longest last finger and compared the difference with their respective sheet resonators with no thickness, obtaining a ratio of frequencies. We found that this ratio of frequencies differed less than $<0.1\%$ among the different resonator line widths. Therefore, we applied this ratio to the remaining 2-dimensional resonators. This way, we obtained values of the simulated thick metal with just simulating the device with no thickness.

Appendix E. Data fitting

The main procedure to fit the data using the iminuit package is already detailed in section 5. Using iminuit one has access to the correlation matrix between variables, which is defined as

$$\rho_{ij} = \frac{\sigma_{ij}}{\sqrt{\sigma_{ii}\sigma_{jj}}}. \tag{E1}$$

[12] This is to be distinguished from the 'Thick metal' model available within Sonnet where no sheet inductance can be defined.

Table 3. table with correlation for fitting of resonator on figure 5(a). Parameters can be seen in equation (10).

	a	α	τ	Q_l	$\lvert Q_\mathrm{c}\rvert$	ϕ	f_r
a	1	0	0	−0.3	−0.3	−0.1	0.1
α	0	1	1	0	0	−0	0
τ	0	1	1	0	0	−0	0
Q_l	−0.3	0	0	1	0.8	0	−0
$\lvert Q_\mathrm{c}\rvert$	−0.3	0	0	0.8	1	0	0
ϕ	−0.1	0	0	0	0	1	−0.7
f_r	0.1	0	0	−0	0	−0.7	1

Here, σ_{ii} is the variance of variable i, and σ_{ij} is the covariance between variables i and j, if $i \neq j$.

When using the fitting formula for the transmission measurements S_{21} equation (10), both quality factors, Q_L and $|Q_\mathrm{c}|$, show high correlation and, indeed, Q_L is bounded by Q_c. Other variables that are highly correlated are f_r with ϕ_0. α and τ are instead fully correlated, given that both appear in the exponential pre-factor of S_{21}. In both cases, a slight change in one of them, provokes adaptations in the other coupled variable to minimize the cost function, which indicates correlation. One could, in principle, parameterize the model in an alternative way to equation (10) to use purely independent variables. However, this parameterization will probably require the use of variables with little physical meaning, thus losing the benefits and information obtained from fitting the variables with actual physical meaning.

In table 3, correlations between parameters are shown for resonator in figure 5(a).

Appendix F. Error propagation

In order to take into account the error introduced in the estimation of λ due to the simulation of the resonator frequencies, we have performed a complete error propagation analysis.

The list of relevant equations already introduced in sections 2 and 3 is the following:

$$L_\mathrm{ks} = \mu_0 \lambda_\mathrm{thin}, \tag{F1}$$

$$\lambda_\mathrm{thin} = \mu_0 \lambda \coth\left(d/\lambda\right), \tag{F2}$$

$$L_\mathrm{k} = N L_\mathrm{ks}, N = g/w, \tag{F3}$$

$$L_\mathrm{k} = L_\mathrm{g}\left(\frac{f_\mathrm{sim}^2}{f_\mathrm{meas}^2} - 1\right). \tag{F4}$$

In order to obtain the error from λ we first obtain the error from λ_thin, as they are connected through an implicit relation, equation (F2). Using equations (F1), (F3) and (F4), λ_thin can be related to our measurable quantities:

$$\lambda_\mathrm{thin} = \frac{w}{\mu_0 g} L_\mathrm{g}\left(\frac{f_\mathrm{sim}^2}{f_\mathrm{meas}^2} - 1\right), \tag{F5}$$

where the resonator inductor width w resonator inductor length g can be obtained by inspection of the devices using scanning electron microscopy, L_g and f_sim can be obtained from finite-element simulation solvers like Sonnet, and, finally, f_meas is measured in the experiment with very high accuracy given by our sophisticated fitting method (see appendix E).

In estimating the errors in the observable quantities, we note that $\delta w \simeq \delta g$, but $\delta w/w \gg \delta g/g$. Therefore we can neglect the error coming from the length, $\delta g \simeq 0$. Also, since our fitting method yields a very accurate value of the measured resonator frequency down to a few kHz, we consider its error negligible compared to the error in the simulated frequency, $\delta f_\mathrm{meas} \simeq 0$. The error from λ_thin can be then computed by differentiation of equation (F5) with respect to w, L_g and f_sim:

$$\delta\lambda_\mathrm{thin} = \frac{1}{\mu_0 g}\left(\frac{f_\mathrm{sim}^2}{f_\mathrm{meas}^2} - 1\right)\left(L_\mathrm{g}\delta w + w\delta L_\mathrm{g}\right) + \frac{2wL_\mathrm{g}}{\mu_0 g}\frac{f_\mathrm{sim}}{f_\mathrm{meas}^2}\delta f_\mathrm{sim}. \tag{F6}$$

Re-arranging terms,

$$\lambda_\mathrm{thin}\left(\frac{\delta w}{w} + \frac{\delta L_\mathrm{g}}{L_\mathrm{g}}\right) + 2\left(\lambda_\mathrm{thin} + \frac{wL_\mathrm{g}}{\mu_0 g}\right)\frac{\delta f_\mathrm{sim}}{f_\mathrm{sim}}. \tag{F7}$$

Therefore, adding the errors in quadrature leads to

$$\frac{\delta\lambda_\mathrm{thin}}{\lambda_\mathrm{thin}} = \left(\left[\left(\frac{\delta w}{w}\right)^2 + \left(\frac{\delta L_\mathrm{g}}{L_\mathrm{g}}\right)^2\right] + 4\left(\lambda_\mathrm{thin} + \frac{wL_\mathrm{g}}{\mu_0 g\lambda_\mathrm{thin}}\right)^2\left(\frac{\delta f_\mathrm{sim}}{f_\mathrm{sim}}\right)^2\right)^{1/2}. \tag{F8}$$

The next step is to calculate the error from λ. To do that we use the relation between observed quantities (λ_thin, d) and inferred (λ) as follows:

$$\lambda_\mathrm{thin} = \lambda \coth\frac{d}{\lambda}. \tag{F9}$$

The error on λ_thin consists of errors on λ and d, which can be obtained by differentiating the expression with respect to each variable:

$$\delta\lambda_\mathrm{thin} = \left[\coth\left(d/\lambda\right) + \frac{d/\lambda}{\sinh^2\left(d/\lambda\right)}\right]\delta\lambda - \frac{\delta d}{\sinh^2\left(d/\lambda\right)}. \tag{F10}$$

Isolating $\delta\lambda$:

$$\delta\lambda = \frac{1}{\coth\left(d/\lambda\right) + \left(d/\lambda\right)\sinh^{-2}\left(d/\lambda\right)} \times \left[\delta\lambda_\mathrm{thin} + \frac{\delta d}{\sinh^2\left(d/\lambda\right)}\right]. \tag{F11}$$

In adding them in quadrature, the total error in λ is

$$\delta\lambda = \frac{1}{\coth\left(d/\lambda\right) + \left(d/\lambda\right)\sinh^{-2}\left(d/\lambda\right)} \times \left[\delta\lambda_\mathrm{thin}^2 + \frac{\delta d^2}{\sinh^4\left(d/\lambda\right)}\right]^{1/2}. \tag{F12}$$

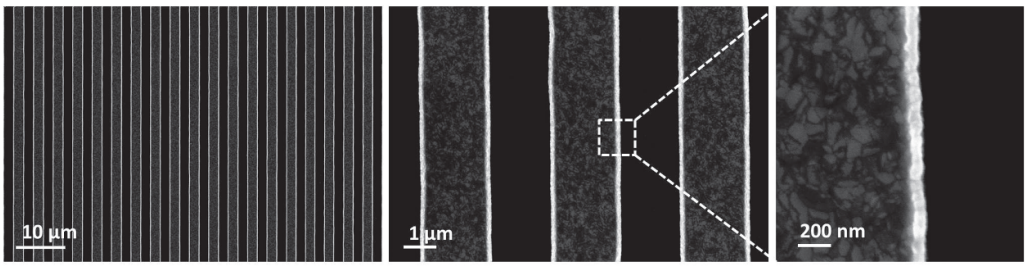

Figure 15. Scanning electron micrograph image of a section of the meander of resonator from device id 8 used in the experiment.

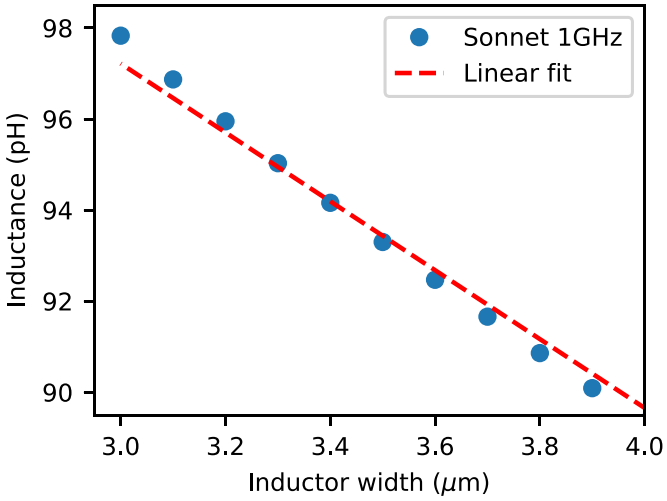

Figure 16. Sonnet simulations of the width dependence of an inductor 150 μm long, 100 nm thick. The slope around 4 μm is $-7.65\text{pH}\,\mu\text{m}^{-1}$.

Equations (F2), (F5), (F8) and (F12) are used to calculate the values of λ_{thin}, λ and their respective errors in table 2 and figures 6 and 7 of the main text.

In order to estimate the error from λ, we need to establish bounds on the errors from the width δw, thickness δd, resonance frequency δf_{sim}, and the simulated geometric inductance δL_{g}.

The bound on width fluctuations has been set to 200 nm based on scanning electron microscope images we have taken from several resonators. Figure 15 shows an example from the meander of resonator from device id 8. Based on the variation of the width, we set $\delta w = 200\,\text{nm}$ as an upper bound. This variation is most likely limited by the resolution of the optical lithography and deposition processes used to fabricate the resonators. This limit on δw is used to set a limit on the error from the simulated resonance frequency, δf_{sim}. By using Sonnet on a simulated resonator circuit and modifying the width of the meander by 100 nm, the resonance is seen to vary on average by 0.6%. Therefore we take $\delta f_{\text{sim}}/f_{\text{sim}} = 0.6\%$. Similarly, the uncertainty in the width is used to set the uncertainty in the value of the simulated geometric inductance, δL_{g}. In order to obtain the sensitivity of width-to-inductance, we simulated an inductor with length (150 μm) and thickness (100 nm) comparable to that of our resonators of varying width around the nominal value of 4 μm, shown in figures 16 and 17 for both Sonnet and COMSOL. The dependence is slightly nonlinear, but the slope in both simulations differs by

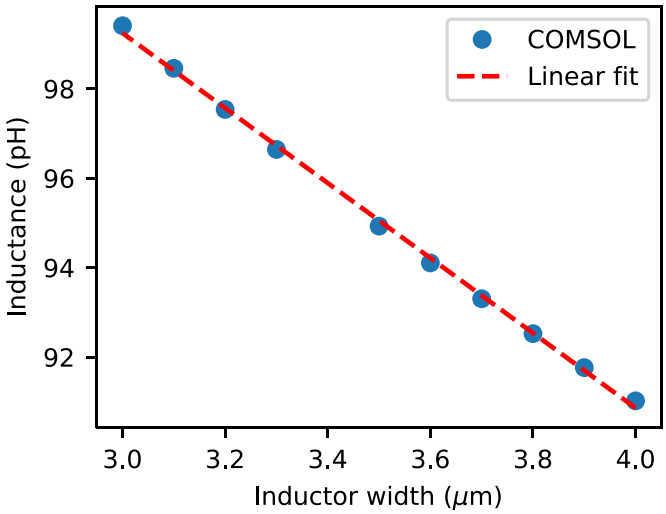

Figure 17. COMSOL simulations of the width dependence of an inductor 150 μm long, 100 nm thick. The slope around 4 μm is $-7.52\text{pH}\,\mu\text{m}^{-1}$.

less than 2% near 4 μm, with a sensitivity of -7.65pH μm^{-1} and -7.52pH μm^{-1} for Sonnet and COMSOL, respectively. Longer meanders give a slightly higher sensitivity, up to 10pH/μm for 200 μm-long meanders. Using this value as un upper bound we obtain a relative error in the inductor of $\delta L_g/L_g = 1\%$. The last error coming from the thickness is taken to be $\delta d = 2$nm, based on AFM images taken from several resonators. The error in the inductance from the uncertainty in the thickness is negligible, as the sensitivity of 16pH μm^{-1} (found from simulations) is of the same order as the sensitivity of the width, but the magnitude of the uncertainty is much smaller.

ORCID iDs

David López-Núñez 0000-0002-5005-3990
Alba Torras-Coloma 0000-0002-9847-8170
Elia Bertoldo 0000-0001-6260-0325
Luca Cozzolino 0000-0002-0548-373X
Giovanni Alberto Ummarino 0000-0002-6226-8518
Alessio Zaccone 0000-0002-6673-7043
Gemma Rius 0000-0003-0552-1043
P Forn-Díaz 0000-0003-4365-5157

References

[1] Cochran J F, Mapother D E and Mould R E 1956 Superconducting transition in aluminum *Phys. Rev.* **103** 1657–69
[2] Brooks M 2023 Quantum computers: what are they good for? *Nature* **617** S1–S3
[3] Kim Y *et al* 2023 Evidence for the utility of quantum computing before fault tolerance *Nature* **618** 500–5
[4] Blais A, Grimsmo A L, Girvin S M and Wallraff A 2021 Circuit quantum electrodynamics *Rev. Mod. Phys.* **93** 025005
[5] Pérez-Salinas A, López-Núñez D, García-Sáez A, Forn-Díaz P and Latorre J I 2021 One qubit as a universal approximant *Phys. Rev. A* **104** 012405
[6] Coiffard G, Daal M, Zobrist N, Swimmer N, Steiger S, Bumble B and Mazin B A 2020 Characterization of sputtered hafnium thin films for high quality factor microwave kinetic inductance detectors *Supercond. Sci. Technol.* **33** 07LT02
[7] Nsanzineza I and Plourde B 2014 Trapping a single vortex and reducing quasiparticles in a superconducting resonator *Phys. Rev. Lett.* **113** 117002
[8] Tinkham M 2004 *Introduction to Superconductivity* (*Dover Books on Physics Series*) (Dover Publications)
[9] Watanabe K, Yoshida K and Kohjiro T A 1994 Kinetic inductance of superconducting coplanar waveguides *Jpn. J. Appl. Phys.* **33** 5708
[10] Forn-Díaz P, Lisenfeld J, Marcos D, García-Ripoll J J, Solano E, Harmans C J P M and Mooij J E 2010 Observation of the Bloch-Siegert shift in a qubit-oscillator system in the ultrastrong coupling regime *Phys. Rev. Lett.* **105** 237001
[11] Weber S J *et al* 2017 Coherent coupled qubits for quantum annealing *Phys. Rev. Appl.* **8** 014004
[12] Gennes P G D 2018 *Superconductivity of Metals and Alloys* (CRC Press)
[13] Mayadas A F 2003 Intrinsic resistivity and electron mean free path in aluminum films *J. Appl. Phys.* **39** 4241–5
[14] Mayadas A F, Feder R and Rosenberg R 1969 Resistivity and structure of evaporated aluminum films *J. Vac. Sci. Technol.* **6** 690–3
[15] Mayadas A F and Shatzkes M 1970 Electrical-resistivity model for polycrystalline films: the case of arbitrary reflection at external surfaces *Phys. Rev. B* **1** 1382–9
[16] Reale C 1974 Thickness and temperature dependence of the critical magnetic field of thin superconducting films of the aluminium group metals *Acta Phys. Acad. Sci. Hung.* **37** 53–60
[17] Gubin A I, Il'in K S, Vitusevich S A, Siegel M and Klein N 2005 Dependence of magnetic penetration depth on the thickness of superconducting nb thin films *Phys. Rev.* B **72** 064503
[18] Yoshida K, Watanabe K, Kisu T and Enpuku K 1995 Evaluation of magnetic penetration depth and surface resistance of superconducting thin films using coplanar waveguides *IEEE Trans. Appl. Supercond.* **5** 1979–82
[19] Rotzinger H, Skacel S T, Pfirrmann M, Voss J N, Münzberg J, Probst S, Bushev P, Weides M P, Ustinov A V and Mooij J E 2016 Aluminium-oxide wires for superconducting high kinetic inductance circuits *Supercond. Sci. Technol.* **30** 025002
[20] Bylander J, Gustavsson S, Yan F, Yoshihara F, Harrabi K, Fitch G, Cory D G, Nakamura Y, Tsai J-S and Oliver W D 2011 Noise spectroscopy through dynamical decoupling with a superconducting flux qubit *Nat. Phys.* **7** 565–70
[21] Wang C *et al* 2014 Measurement and control of quasiparticle dynamics in a superconducting qubit *Nat. Commun.* **5** 5836
[22] Pippard A B and Bragg W L 1953 An experimental and theoretical study of the relation between magnetic field and current in a superconductor *Proc. R. Soc. A* **216** 547–68
[23] Mattis D C and Bardeen J 1958 Theory of the anomalous skin effect in normal and superconducting metals *Phys. Rev.* **111** 412–7
[24] Kautz R L 2008 Picosecond pulses on superconducting striplines *J. Appl. Phys.* **49** 308–14
[25] Turneaure J P, Halbritter J and Schwettman H A 1991 The surface impedance of superconductors and normal conductors: the Mattis-Bardeen theory *J. Supercond.* **4** 341–55
[26] Faber T E and Pippard A B 1955 The penetration depth and high-frequency resistance of superconducting aluminium *Proc. R. Soc. A* **231** 336–53
[27] Meservey R H and Tedrow P M 1971 Properties of very thin aluminum films *J. Appl. Phys.* **42** 51–53
[28] Saint-James D, Sarma G, Thomas E J and Silverman P 1969 *Type II Superconductivity* (Pergamon)
[29] Abrikosov A A 1957 Magnetic properties of superconductors of the second group *Sov. Phys. - JETP* **5** 1174 (Engl. transl.)
[30] Pearl J 2004 Current distribution in superconducting films carrying quantized fluxoids *Appl. Phys. Lett.* **5** 65–66
[31] Ashkroft N M N 1976 *Solid State Physics* (Brooks/Cole)
[32] Romijn J, Klapwijk T M, Renne M J and Mooij J E 1982 Critical pair-breaking current in superconducting aluminum strips far below T_c *Phys. Rev. B* **26** 3648–55
[33] Krupka J, Breeze J, Centeno A, Alford N, Claussen T and Jensen L 2006 Measurements of permittivity, dielectric loss tangent and resistivity of float-zone silicon at microwave frequencies *IEEE Trans. Microw. Theory Tech.* **54** 3995–4001
[34] O'Connell A D *et al* 2008 Microwave dielectric loss at single photon energies and millikelvin temperatures *Appl. Phys. Lett.* **92** 112903
[35] We use high-resistivity (1-0-0) intrinsic Si wafers from Topsil with measured resistivity values above 100kΩ·cm and

spurious doping of Phosphorous/Boron below 1×10^{11} atoms/cm^3. Carbon and Oxygen verified to be below FTIR detection limits of 10^{15} atoms/cm^3

[36] Doyle S, Mauskopf P D, Naylon J A, Porch A and Duncombe C 2008 Lumped element kinetic inductance detectors *J. Low Temp. Phys.* **151** 530–6

[37] Probst S, Song F B, Bushev P A, Ustinov A V and Weides M 2015 Efficient and robust analysis of complex scattering data under noise in microwave resonators *Rev. Sci. Instrum.* **86** 024706

[38] Dembinski H *et al* 2020 scikit-hep/iminuit *Zenodo* (https://doi.org/10.5281/zenodo.3949207)

[39] Maleeva N *et al* 2018 Circuit quantum electrodynamics of granular aluminum resonators *Nat. Commun.* **9** 3889

[40] Brandt B L, Parks R D and Chaudhari R D 1971 Intermediate state of thin superconductors *J. Low Temp. Phys.* **4** 41–63

[41] Stan G, Field S B and Martinis J M 2004 Critical field for complete vortex expulsion from narrow superconducting strips *Phys. Rev. Lett.* **92** 097003

[42] Pan X *et al* 2022 Engineering superconducting qubits to reduce quasiparticles and charge noise *Nat. Commun.* **13** 7196

[43] Li K, Dutta S K, Steffen Z, Poppert D, Keshvari S, Bowser J, Palmer B S, Lobb C J and Wellstood F C 2022 Long-lived transmons with different electrode layouts *MRS Adv.* **7** 273–7